Decadal Variability in the South Pacific Subtropical Countercurrent and Regional Mesoscale Eddy Activity

SETH TRAVIS AND BO QIU

University of Hawai'i at Mānoa, Honolulu, Hawaii

(Manuscript received 21 September 2016, in final form 18 December 2016)

ABSTRACT

Decadal variability of eddy activity in the western, subtropical South Pacific is examined using the past two decades of satellite altimetry data. Between 21° and 29°S, there is a band of heightened eddy activity. In this region, the eastward South Pacific Subtropical Countercurrent (STCC) overlays the westward South Equatorial Current (SEC). This vertically sheared STCC–SEC system is subject to baroclinic instabilities. By using the European Centre for Medium-Range Weather Forecasts (ECMWF) Ocean Reanalysis System, version 4 (ORAS4), data and verifying with the gridded Argo float data, low-frequency variations in the state of the ocean in this region are investigated. It is found that the low-frequency changes in the shearing and stratification of the STCC–SEC region simultaneously work to modulate the strength of baroclinic instabilities, as measured through the baroclinic growth rate. These changes in the strength of the instabilities consequently affect the observed eddy activity. Using a linearization of the baroclinic growth rate, the contribution to the variability from the changes in shearing is found to be roughly twice as large as those from changes in stratification. Additionally, changes in the temperature and salinity fields are both found to have significant impacts on the low-frequency variability of shearing and stratification, for which salinity changes are responsible for 50%–75% of the variability as caused by temperature changes. However, the changes in all these parameters do not occur concurrently and can alternately work to negate or augment each other.

1. Introduction

The South Pacific Subtropical Countercurrent (STCC) is an eastward-moving current, manifesting as a band starting to the north of New Zealand and extending into the open South Pacific. First identified as the South Tropical Countercurrent (Merle et al. 1969), additional studies have also described the flow in this region as a shallow component of the northern edge of the eastward subtropical gyre circulation (e.g., Wyrtki 1975; Tsuchiya 1982). This broadly shallow current, hereafter referred to as the STCC, manifests from a vertical spreading of isopycnals, creating a reversal of the westward shearing of the South Equatorial Current (SEC) at depth to an eastward shearing in the upper ocean (Reid 1986; De Szoeke 1987; Qu and Lindstrom 2002). While the current is relatively weak as compared to other currents in the region, such as the East Australia Current, it is nonetheless a region of heightened eddy activity, as seen in the red box in Fig. 1a. Previous studies have explored the source of the heightened eddy activity found in the region as being caused by baroclinic instabilities (Qiu and Chen 2004).

Qiu and Chen explored the seasonal variation of the eddy kinetic energy (EKE) in this region. They found that variations in the strength of baroclinic instabilities, as calculated through the baroclinic growth rate, were the most likely cause for the seasonality of the EKE and emphasized the seasonal change in the zonal shearing between the STCC and the SEC as the primary factor of the seasonal variability in baroclinic growth rates. Perhaps unsurprisingly, variations in the observed EKE patterns likely depend strongly upon the state of the STCC and the SEC. Qiu and Chen (2006) and Roemmich et al. (2007) observed a decadal spinup of the South Pacific Subtropical Gyre and attributed the spinup to an increased wind stress curl over the larger ocean basin during the 1990s. More recently, Zhang and Qu (2015) found that the gyre spinup has continued through the study period to 2013, causing an increase in SEC transport by 20%–30%. This spinup has a number of possible consequences for the STCC–SEC region. In addition to the changes in shearing caused by increased transport, the redistribution of water characteristics could affect the

Corresponding author e-mail: Seth Travis, stravis3@hawaii.edu

DOI: 10.1175/JPO-D-16-0217.1

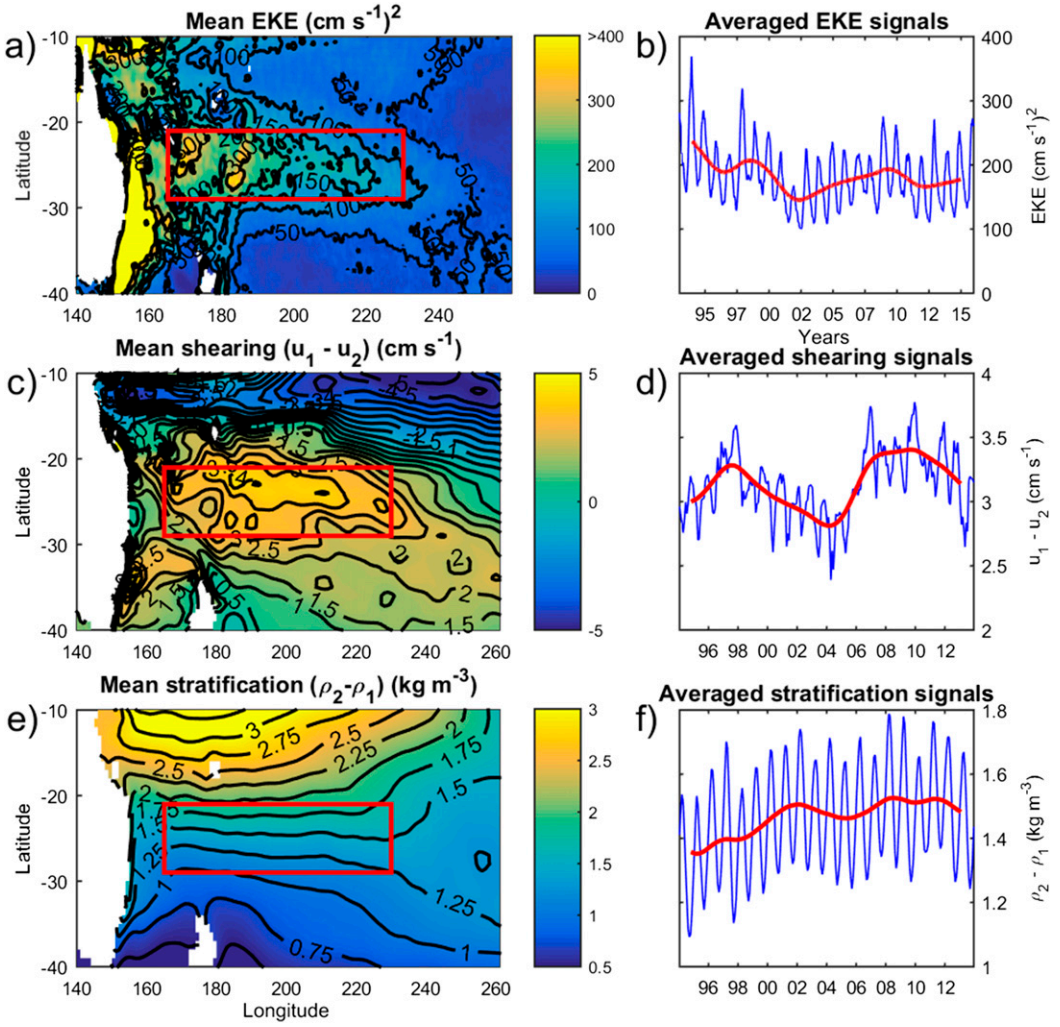

FIG. 1. (left) Mean state of the South Pacific. The STCC region is outlined by the red box. (right) Area-averaged signals of the STCC region. The low-pass signal ($<1\,\mathrm{yr}^{-1}$) is given in the solid red line. (top) EKE ($\mathrm{cm}^2\,\mathrm{s}^{-2}$). (middle) Shearing ($\mathrm{cm}\,\mathrm{s}^{-1}$). (bottom) Stratification ($\mathrm{kg}\,\mathrm{m}^{-3}$).

stratification in the region. For example, Schneider et al. (2007) found that the spinup of the gyre freshens and cools the eastern South Pacific, while also showing a significant warming trend in the western South Pacific. Additionally, Sasaki et al. (2008) found that the basin-scale spinup causes changes in the eddy activity in the Tasman Front, focusing on the area just to the southwest of the STCC–SEC region. These broad patterns affecting South Pacific Subtropical Gyre circulation could manifest in the STCC–SEC region, altering the state of the ocean and leading to enhanced eddy activity.

An increasingly long record of observations in the region allows us to improve our understanding of the basic state of the STCC–SEC region and the slow, decadal variability from this mean state. This paper works to expand upon those previous findings by providing a detailed description of the basic state of the ocean, which promotes eddy activity, and then proceeding to describe longer-term, decadal variations in the EKE signal and within the STCC–SEC itself (see Fig. 1). Following the work by Qiu and Chen (2004), using an idealized model of the region as a 2.5-layer, baroclinic system, the strength of the instabilities can be simply parameterized. Variations in the strength of the instabilities should cause similar variations in the strength of the eddies, as measured through EKE. The variability of shearing and stratification in the region can be measured and used to calculate fluctuations in the strength of baroclinic instabilities, as given through the baroclinic growth rate. Additionally, efforts are made to quantify the amount of variation that can be

attributed to the shearing and stratification parameters and the relative influence on these of temperature versus salinity signals.

2. Datasets

The AVISO merged satellite, ¼° × ¼° gridded, daily mean product is a source of more than 20 yr of data for sea surface height (Ducet et al. 2000). Covering the time frame from 1993 to present, this dataset can be used to examine a number of oceanographic features. Apart from measuring changes in the absolute sea surface height, sea surface height anomalies can also be used to calculate anomalous geostrophic velocities and in turn quantify the EKE in the STCC region.

Depth profiles of horizontal velocities, temperature, and salinity data from the European Centre for Medium-Range Weather Forecasts (ECMWF) Ocean Reanalysis System, version 4 (ORAS4), are used (Balmaseda et al. 2013). The data product provides a 1° × 1° gridded, monthly mean data product, running from 1957 to present. This provides a data record that covers the entirety of the AVISO satellite altimetry dataset and our subsequent EKE calculations. For verification of the product, additional data are taken from Argo profiling floats, using the Grid Point Value of the Monthly Objective Analysis (MOAA GPV) dataset, as compiled by Hosoda et al. (2008). The MOAA GPV data product provides a 1° × 1° gridded, monthly mean data product of profiles of temperature and salinity. These profiles extend down to 2000-m depth. By assuming a thermal wind balance, these profiles can be used to calculate the vertical shearing of the horizontal ocean currents. Argo floats have provided observational subsurface information since 2001. Starting in 2004, there begins to be sufficient Argo float coverage in the South Pacific for relatively good measurements of the ocean state and its variability. This data will be used for comparison against the ECMWF ORAS4 data. It should be noted that as the ORAS4 utilizes Argo data in its reanalysis, it is not a fully independent dataset, and as such the comparison between the datasets cannot be used to fully corroborate the findings before 2004.

As shown in Fig. 2, the averaged signal of shearing is very similar in the Argo and ECMWF datasets. This is also true of the averaged stratification signal. Here, u_1 and u_2 are defined as the depth-averaged zonal velocity of the upper 200 m of the ocean and between 200 and 600 m, respectively. Likewise, ρ_1 and ρ_2 are the depth-averaged density of each layer. The area-averaged time signal is able to capture the low-frequency ($<1\,\mathrm{yr}^{-1}$) variability as well as a large amount of the seasonal variability. Generally, the Argo data show a slightly less sheared and a slightly more stratified system. Both of these factors would contribute to make the system less baroclinically unstable in the Argo data. In addition to the time variability signals, the vertical profiles are also very similar. The only level at which there is any discrepancy of note is at the very surface of the profile of zonal current. In these profiles, the surface zonal currents in the Argo profile continue to strengthen the eastward flow, whereas the ECMWF profile actually has a slightly more westward flow. This difference can be understood from the lack of Ekman flows in the Argo-based calculations, resulting in a slight overestimation of the near-surface zonal velocity in the Argo time series.

Figure 3 shows the low-pass filtered, meridionally averaged variability in the two datasets. As in the time series and vertical profiles, there is high agreement between the two datasets. In both the shearing and stratification, the Argo and ECMWF data exhibit the same patterns of highs and lows, with only minor variations in exact location and timing. The largest discrepancies between the two datasets come from the magnitude of some of the changes. Generally, data from ECMWF have larger anomalies than that of the Argo data. However, overall there is strong agreement between the data series, which gives confidence that the ECMWF data are capturing the dynamics of the region and that this data can be used to extend the data record over the full period spanning the AVISO altimetry data record.

3. Observations

The analyses are confined to the band of 21°–29°S, 165°E–130°W, as indicated by the red boxes in each of the maps in Fig. 1. This is the band of the highest eddy activity and is where the STCC and SEC have the strongest interactions. To explore changes in the region, satellite altimetry data will be used to look at eddy activity, while ECMWF ORAS4 data are used to examine depth profiles of velocity, density, temperature, and salinity.

a. *EKE observations*

Satellite data reveal the elevated eddy activity across the STCC region. The STCC region has an annual EKE cycle that averages $+60/-50\,\mathrm{cm}^2\,\mathrm{s}^{-2}$. The region has a mean EKE greater than $150\,\mathrm{cm}^2\,\mathrm{s}^{-2}$ across most of the region, with the western region exceeding a mean level of $200\,\mathrm{cm}^2\,\mathrm{s}^{-2}$. (Figs. 1a,b) Within this band, there are particularly active regions near 170°E, and 182°–187°E. These correspond to the seamount ridges of the Norfolk Ridge for the western band and the Kermadec and Colville Ridges, which surround the Lau Basin, for the eastern band. In these sites, the mean EKE can exceed $350\,\mathrm{cm}^2\,\mathrm{s}^{-2}$.

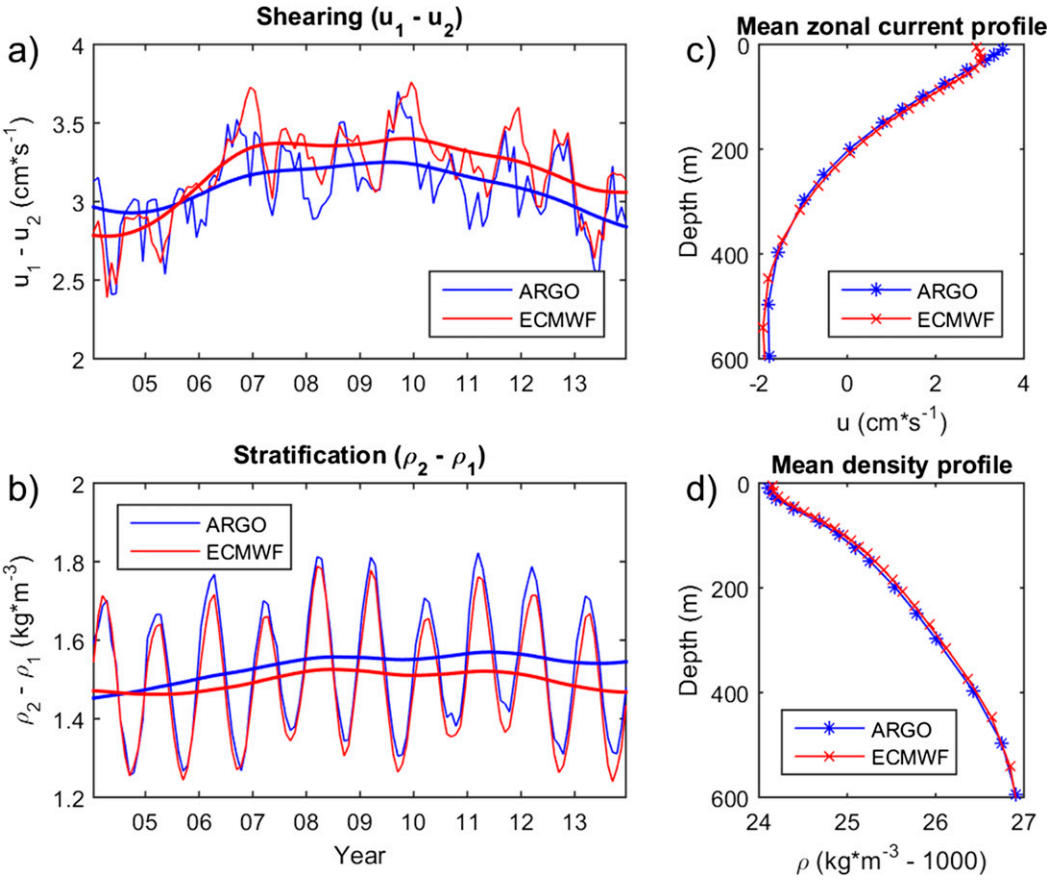

FIG. 2. Time series of the (a) averaged shear and (b) stratification in the Argo and ECMWF datasets. Averaged vertical profiles of (c) zonal current and (d) density.

For analysis, meridionally averaged bands of properties in the STCC–SEC region are used to look at the spatial and temporal patterns. These properties are EKE, shearing, stratification, temperature, and salinity. It is found that for the low-pass filtered signal ($<1\,\mathrm{yr}^{-1}$), the meridionally averaged signal shows high correlation with the signal at any point and is representative of the whole band. The low-pass filtered EKE values vary by nearly $\pm 75\,\mathrm{cm}^2\,\mathrm{s}^{-2}$, which is comparable in magnitude to the seasonal variability (Fig. 4a). The patterns show significant spatial variability. A rough description of the variability would first break the region into an eastern half and a western half (east/west of 195°E). In these patterns, the east experiences higher EKE from 1993 to 2001 and a short period between 2005 and 2008. In the west, there is a short high-EKE period from 1993 to 1997 and from 2007 to 2012. It is these long-term patterns that are hypothesized to be caused by changes in the strength of the baroclinic instabilities. The spatial–temporal patterns of long-term changes in the baroclinic growth rate will need to exhibit similar patterns in order to verify the hypothesis that these variations are the primary driver of changes in eddy activity.

b. *Shearing*

To first approximate the vertically sheared STCC–SEC system, a 2.5-layer model is utilized. The model is set up with a light, eastward-flowing top layer; a heavy, deeper, westward-flowing layer; and a quiescent bottom layer. The depth of the upper layer is chosen as 200 m. This is the mean depth of flow reversal, from which the currents switch from being eastward to westward with increasing depth. For the lower layer, a mean depth of 600 m (400 m layer thickness) is chosen, as this is the depth at which the mean shear changes from positive (eastward) to negative (westward). As a test, ventilated thermocline theory (Luyten et al. 1983) is used to calculate the respective layer depths for a similarly layered ocean. Using reference layer densities of $\rho_1 = 1024.75\,\mathrm{kg\,m}^{-3}$, $\rho_2 = 1026.4\,\mathrm{kg\,m}^{-3}$, $\rho_3 = 1027.25\,\mathrm{kg\,m}^{-3}$, and the mean wind stress curl field across the South Pacific, the layer thickness averaged in

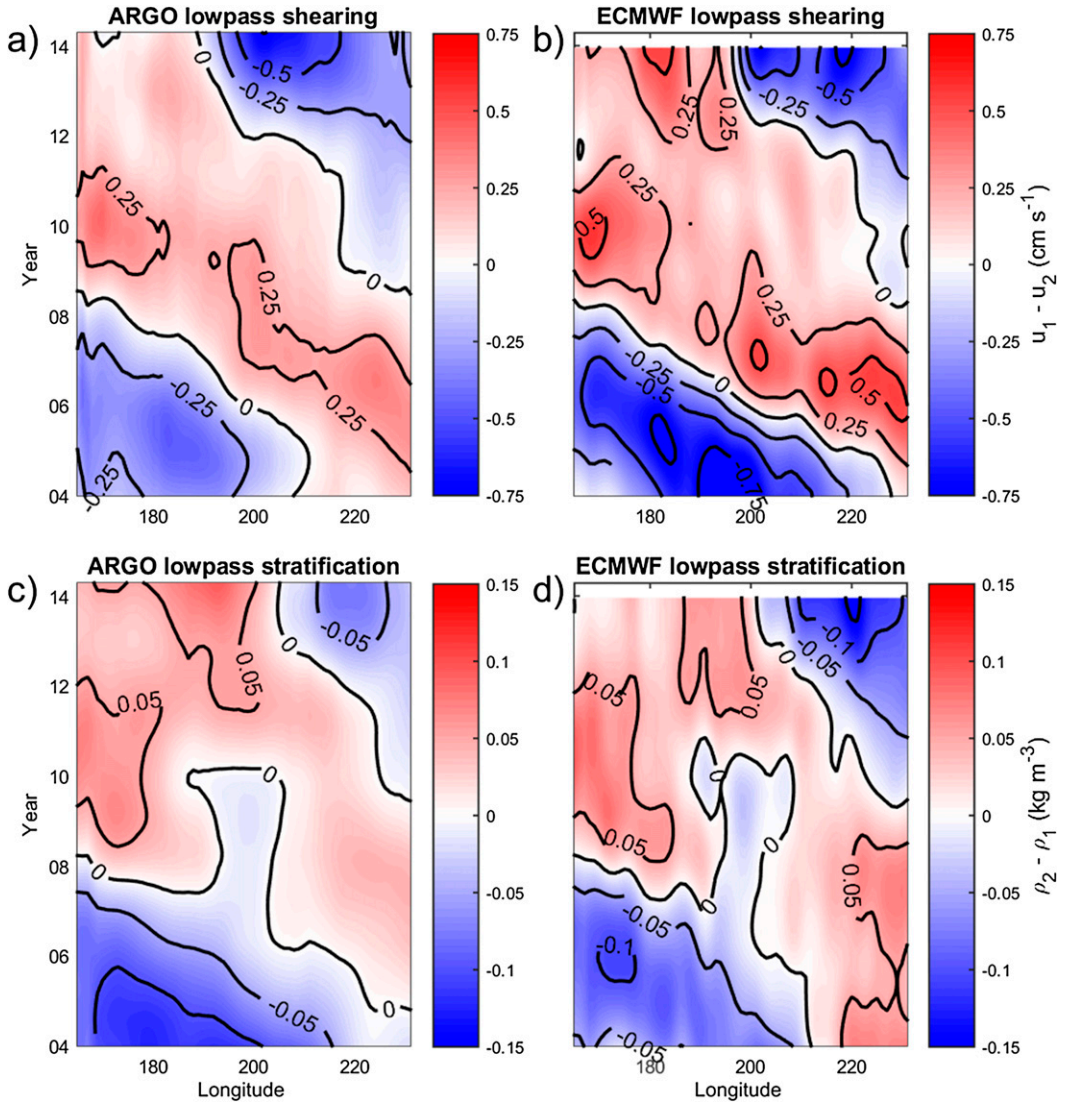

FIG. 3. Meridionally averaged low-pass bands of (top) shear and (bottom) stratification in the (left) Argo and (right) ECMWF datasets.

the STCC region is found to be 200–250 m for the upper layer and approximately 400 m for the lower layer. This corresponds quite well to our initial approximation of the two layer thicknesses. Within each of the layers, the density and velocity are taken as the depth-averaged value of the respective parameter.

Now using our representation of the STCC–SEC region, the shearing of the 2.5-layer system can be represented by the velocity difference between the two layers. This is the same representation of the shearing as used in section 2, where the shearing is defined as $U_1 - U_2$, and U_1 and U_2 are the depth-averaged zonal velocity of each respective layer. The shearing experienced in the region depends upon the relative strengths of the STCC and the SEC, which manifest as the underlying current below the STCC and are components of the wind-driven South Pacific Gyre circulation. For the mean state, the strongest shearing occurs to the north, exceeding 3.5 cm s^{-1} for much of the area. In the southern regions, the mean shearing is between 2.5 and 3.5 cm s^{-1} (Figs. 1c,d).

As shown in Fig. 4b, the low-pass filtered shearing signal varies in excess of ± 0.5 cm s^{-1} for much of the region. This range, being greater than 1.0 cm s^{-1} in strength, is on the same order of magnitude as the seasonal cycle. Roughly speaking, the eastern half of the region experiences highs from 1993 to 1999 and 2006 to 2012, while the western half experiences a

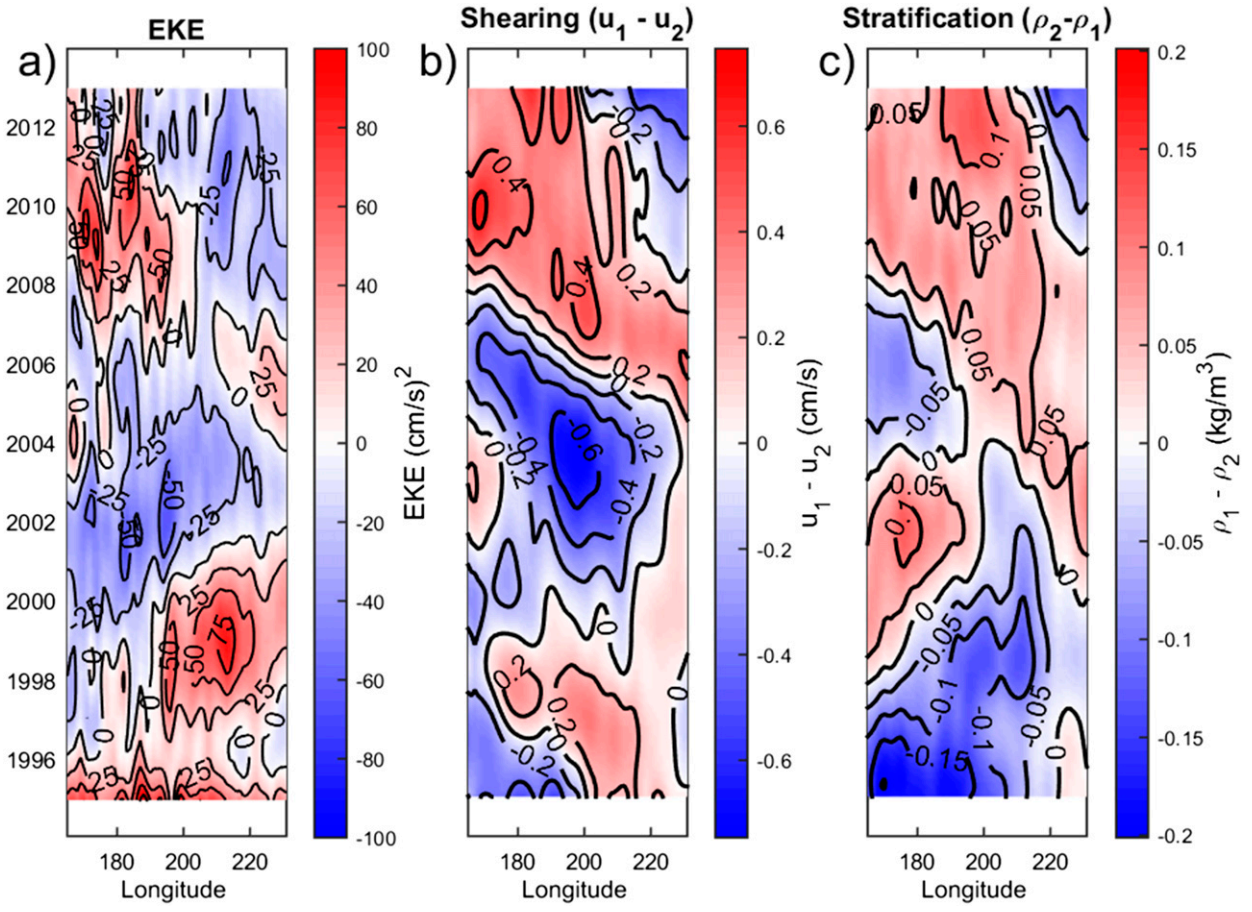

FIG. 4. Meridionally averaged bands of low-pass (<11 yr^{-1}) variation in the STCC. (a) EKE (cm^2 s^{-2}). (b) Shearing (cm s^{-1}). (c) Stratification (kg m^{-3}).

relatively minor high from 1998 to 2004 and a stronger high from 2008 to 2014.

c. *Stratification*

Just as with the shearing in the STCC–SEC region, the stratification can be simply described as the density difference between the two layers. This is given by $\rho_2 - \rho_1$, where ρ_1 and ρ_2 are the depth-averaged densities of the respective layers. The mean density difference between the two layers is 1.5 kg m^{-3}, exceeding 1.8 kg m^{-3} to the north, and as low as 1 kg m^{-3} to the south (Figs. 1e,f). There is a very strong seasonal cycle in the stratification. The majority of this seasonal cycle can be accounted for through the warming and cooling of the upper waters as the seasons change. This seasonal cycle has a range of 0.4–0.5 kg m^{-3}.

Low-frequency variation has mostly led to an increased level of stratification over the last 22 yr (see Fig. 4c). This is accounted for primarily through the lightening of the upper waters. The average stratification has increased by roughly 0.15 kg m^{-3} over this time period, equaling 30% of the seasonal variation and a greater than a 10% increase of the mean state. The fluctuations in stratification can exceed $\pm$0.1 kg m^{-3} over the whole time range. The majority of this variability occurs, again, in the upper layer. While there is some slight variability in the deeper layer, it has maximum departures from the mean state of 0.05 kg m^{-3}, roughly one-third of the total change. To understand the primary drivers of the changes in the stratification, looking at changes in the upper layer will provide the greatest insight.

d. *Change in the state of the STCC*

By focusing our analysis on the changing state of the upper layer, through temperature and salinity fluctuations, we are able to discover more about the driving forces in the region. Stratification variability is directly explored through the changing of the upper-layer density, using a linearized state equation for density of $\rho = \rho_0 - \alpha_T(T - T_0) + \beta_S(S - S_0)$, where the zero subscript indicates the mean state; T and S are the depth-averaged temperature and salinity of the

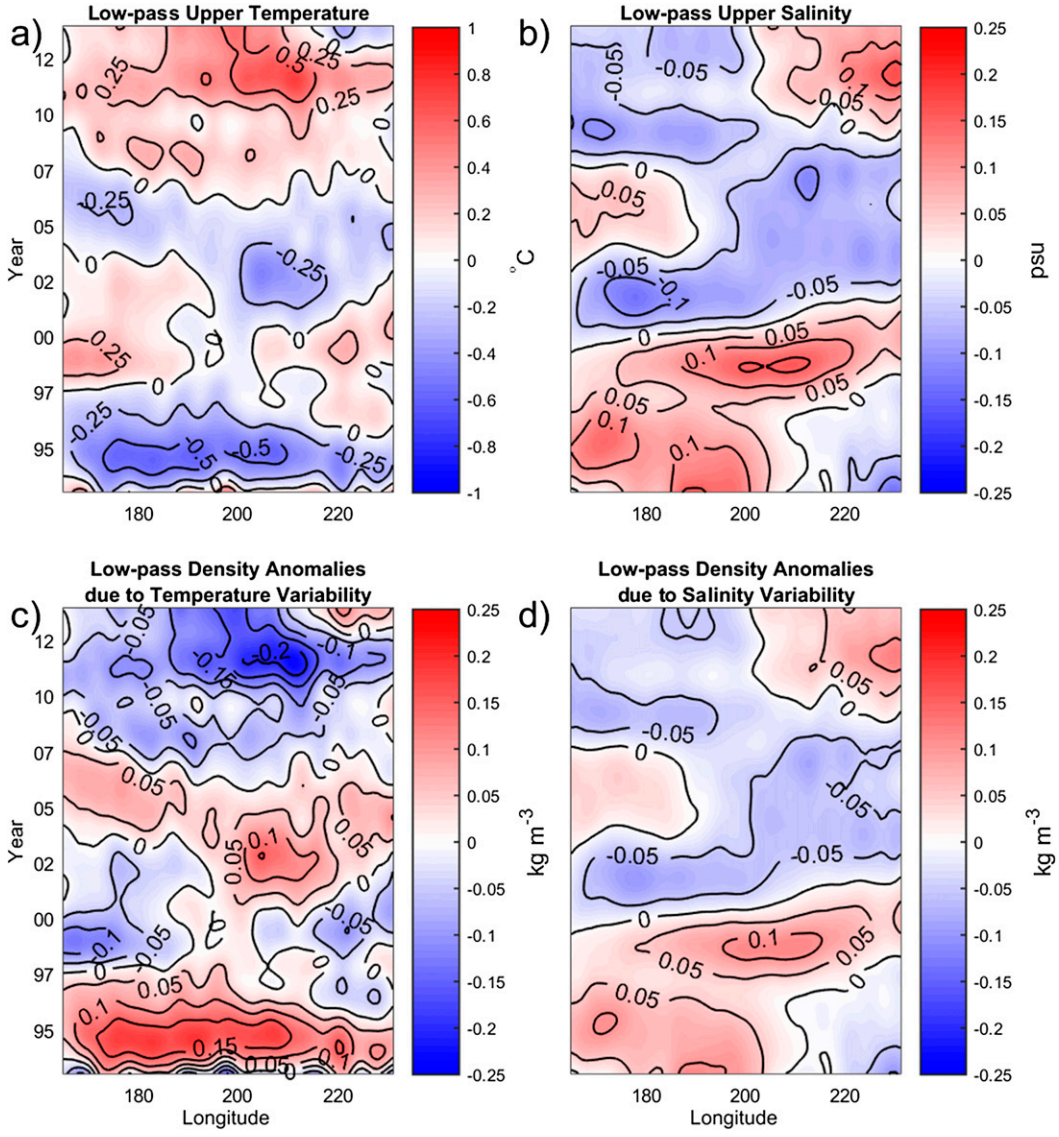

FIG. 5. Meridionally averaged bands of (top) temperature and salinity variations and (bottom) density anomalies caused by varying temperature and salinity. Low-pass (a) temperature (°C) and (b) salinity (psu). Low-pass density (kg m^{-3}) with (c) varying temperature and fixed salinity and (d) varying salinity and fixed temperature.

upper layer; α_T and β_S are thermal expansion and haline contraction coefficients, respectively; and ρ_0 is the mean density of the upper layer. Shear variability is explored using a similar state equation while also applying a thermal wind balance and integrating through the layer. In this case, the upper-layer zonal velocity is given by $U=U_0+[(gH_1)/\rho_0 f]\{-\alpha_T[\partial(T-T_0)/\partial y]+\beta_S[\partial(S-S_0)/\partial y]\}$, where U_0 is the mean zonal velocity of the upper layer, and H_1 is the layer thickness of the upper layer.

Temperature fluctuations are the dominant factor in the seasonality of density fluctuations. When holding salinity constant, temperature fluctuations can cause a density change of 0.5 kg m^{-3} in the upper layer of the ocean. The low-frequency change in temperature shows a regionwide warming (Fig. 5a). From 1993 to 2013, there is roughly a 0.5°C increase in the upper-layer temperature, which is more than double the rate of the globally average sea surface temperature rise of 0.11°C decade^{-1} for the upper 75 m (IPCC 2013). This high warming causes a decrease in layer density by 0.2–0.3 kg m^{-3}, as can be seen in Fig. 5c. Density changes caused by temperature variability in the upper layer are highly correlated, at a correlation of 0.83, to changes in the total layer density variability.

Figure 6a shows the anomalous meridional temperature gradients, with the resultant zonal velocity anomalies

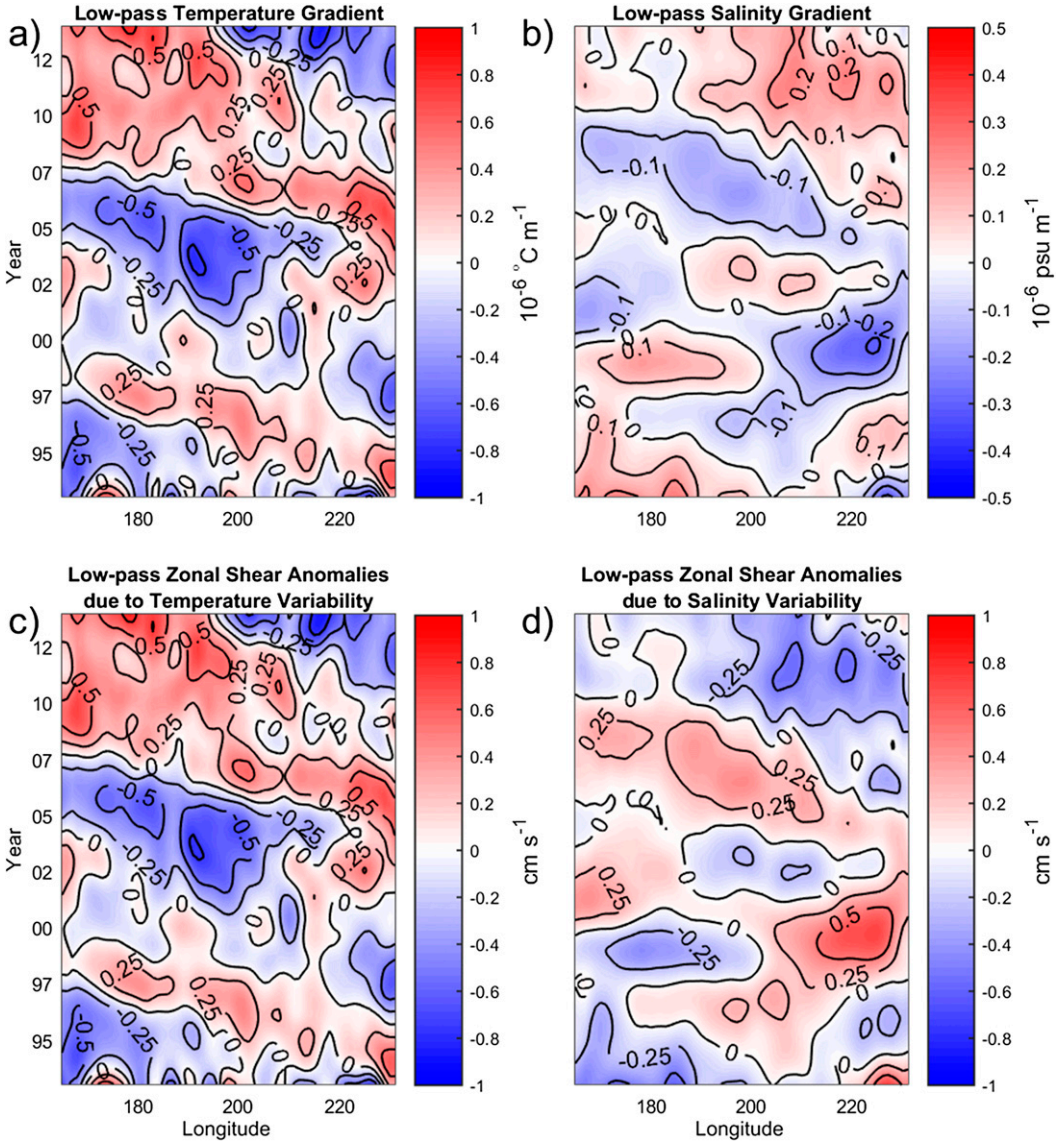

FIG. 6. Meridionally averaged bands of variations in the meridional gradient of (top) temperature and salinity and (bottom) the meridional density gradient anomalies caused by varying temperature and salinity. Low-pass gradient of (a) temperature (°C m^{-1}) and (b) salinity (psu m^{-1}). Low-pass velocity anomalies (cm s^{-1}) derived from (c) varying temperature and fixed salinity and (d) varying salinity and fixed temperature.

caused by the density gradients shown in Fig. 6c. The zonal velocity anomalies can exceed ± 0.5 cm s^{-1} and is approximately equal in magnitude to the changes in the shearing in the STCC–SEC region. There is a high correlation of 0.84 between the shearing and the temperature-induced zonal velocity anomalies.

Seasonal salinity fluctuations are negligible when compared to the temperature fluctuations. Seasonal fluctuations of only 0.02 psu are responsible for a 0.01 kg m^{-3} change in density, which is only 2% of that caused by temperature fluctuations. This minute fluctuation can largely be ignored. However, the low-frequency salinity fluctuations are significant. The salinity varies by as much as 0.25 psu over the time period, as seen in Fig. 5b. This results in density anomalies up to as much as 0.15 kg m^{-3}, shown in Fig. 5d. These fluctuations are roughly 50%–75% of those temperature-caused density anomalies and are not negligible. When compared to the variations in the upper-layer density, there is a modest correlation with the salinity-induced density variability of 0.69.

The zonal velocity changes caused by salinity variability are smaller. The changing salinity field results in velocity changes of ± 0.25 cm s^{-1}, with some patchy areas that can exceed ± 0.5 cm s^{-1} (Fig. 6d). This is about 50% of the

velocity changes caused by temperature variability and has a very low correlation of 0.04. The salinity-induced zonal velocity changes are nearly entirely out of phase with those of the more dominant temperature-induced changes.

There is previous work that has looked at changes in the salinity patterns across the South Pacific. Zhang and Qu (2014) explored a freshening of South Pacific Tropical Water (SPTW), which has a salinity maximum to the northeast of the STCC–SEC region of high eddy activity. They found a poleward shift of the salinity maximum, with sea surface salinities (SSS) along the northern section of the formation region being advected by the SEC. They also note a strong correlation of SSS to the Pacific decadal oscillation (PDO). Schneider et al. (2007) examined changes in the salinity fields due to the spinup of the South Pacific Gyre, in which the increased circulation brings colder, fresher, subantarctic waters farther north.

From these results, it can be said that temperature fluctuations are the major driver of variability in the state of the STCC–SEC region. Changes in the shearing and stratification induced by temperature variability are generally about twice as large as those caused by salinity variability. However, the salinity variability is not negligible. Changes induced by salinity variability largely work to modulate those of temperature variability and negate some of the largest temperature-induced fluctuations. In rare cases, the two parameters can work in phase with each other and cause some of the greatest variability in shear and stratification. An example of this can be seen in the shear signal in the middle of the STCC–SEC region between 2002 and 2005 (see Figs. 6c,d, 4b). Both the X temperature and salinity variability cause negative zonal velocity anomalies, albeit of different magnitudes, and together create the weakest shearing across the STCC–SEC region over the time record.

4. Baroclinic instability growth rates

If the eddy activity in the region is the result of baroclinic instabilities, then calculating and analyzing shifts in how unstable the system is should correspond well to the shifts in the eddy activity. In understanding the baroclinic instability growth rate, the instability criterion given below tells us that the shearing of the layers must exceed the baroclinic Rossby wave speed plus a scaled advection by the lower layer. The criterion can be derived by following the same process as Qiu (1999):

$$U_1 - U_2 > \frac{(\rho_2 - \rho_1) g H_2}{\rho_1 f_0^2}\beta + \gamma_2 U_2, \qquad (1)$$

where $\gamma_2 = (\rho_2 - \rho_1)/(\rho_3 - \rho_2)$, $[\rho_1, \rho_2, \rho_3]$ is the density of their respective layers, g is the gravitational constant, H_2 is the mean lower-layer thickness, f_0 is the Coriolis parameter at a reference latitude (in this case 25°S), and $\beta = df/dy$ is the beta parameter at the reference latitude. For derivations, see Eq. (16) in Qiu (1999).

From Eq. (1), we can tell that the shearing and the stratification are important parameters. Measuring the strength of baroclinic instabilities is done by calculating the peak baroclinic instability growth rate. As the degree of instability is a nonlinear process, it is expected that proportional changes in shearing or stratification do not necessarily result in proportional changes in the baroclinic growth rate. In Fig. 7a, the baroclinic growth rate for a range of shearing and stratification scenarios is shown, where the red box indicates the average seasonal range of shearing and stratification for all areas in the STCC–SEC region, while the green line indicates the area-averaged seasonal cycle. As shearing increases, so does the baroclinic growth rate. Conversely, decreasing stratification leads to an increase in the baroclinic growth rates.

While the peak baroclinic growth rate is a nonlinear calculation, it is possible to linearize the growth rate around some reference state. By doing this, we are able to tease out the relative importance of the shearing and stratification in affecting the strength of the baroclinic instability. Assuming that changes in the baroclinic growth rate are locally linear at some reference level, after using a Taylor expansion, the baroclinic growth rate can be given by the following equation:

$$\sigma = \sigma_0[1 + \alpha(\rho_z - \rho_{z0}) + \gamma(U_z - U_{z0})]. \qquad (2)$$

In Eq. (2), U_z is the shear or velocity difference between the layers, ρ_z is the stratification or density difference between the layers, σ is the baroclinic growth rate, and U_{z0}, ρ_{z0}, and σ_0 are the reference values for the respective terms. The terms α and γ are parameters determined by the local derivative of the baroclinic growth rate at the reference levels, scaled by the reference baroclinic growth rate. They are calculated as $\alpha = [(\partial\sigma/\partial U_z)|_{\rho_{z0}}]/\sigma_0$ and $\gamma = [(\partial\sigma/\partial\rho_z)|_{U_{z0}}]/\sigma_0$. The mean state, spatially and temporally, was used for the reference levels. For the STCC–SEC region, the mean state is $U_{z0} = 3.1\,\mathrm{cm\,s^{-1}}$, and $\rho_{z0} = 1.45\,\mathrm{kg\,m^{-3}}$, giving a reference baroclinic growth rate of $\sigma_0 = 0.0101\,\mathrm{day^{-1}}$.

Figures 7c and 7d show the linear rate of change, proportional to the reference baroclinic growth rate σ_0, for changing stratification and shearing (i.e., α and γ), respectively. Figure 7c gives estimates of possible values of α, the stratification parameter. Within the range of variation across the STCC–SEC region, as indicated in the red box, α has a typical value of -0.9. Similarly, in Fig. 7d, the shearing parameter γ has typical values of 0.35. These reference parameters will be used in the

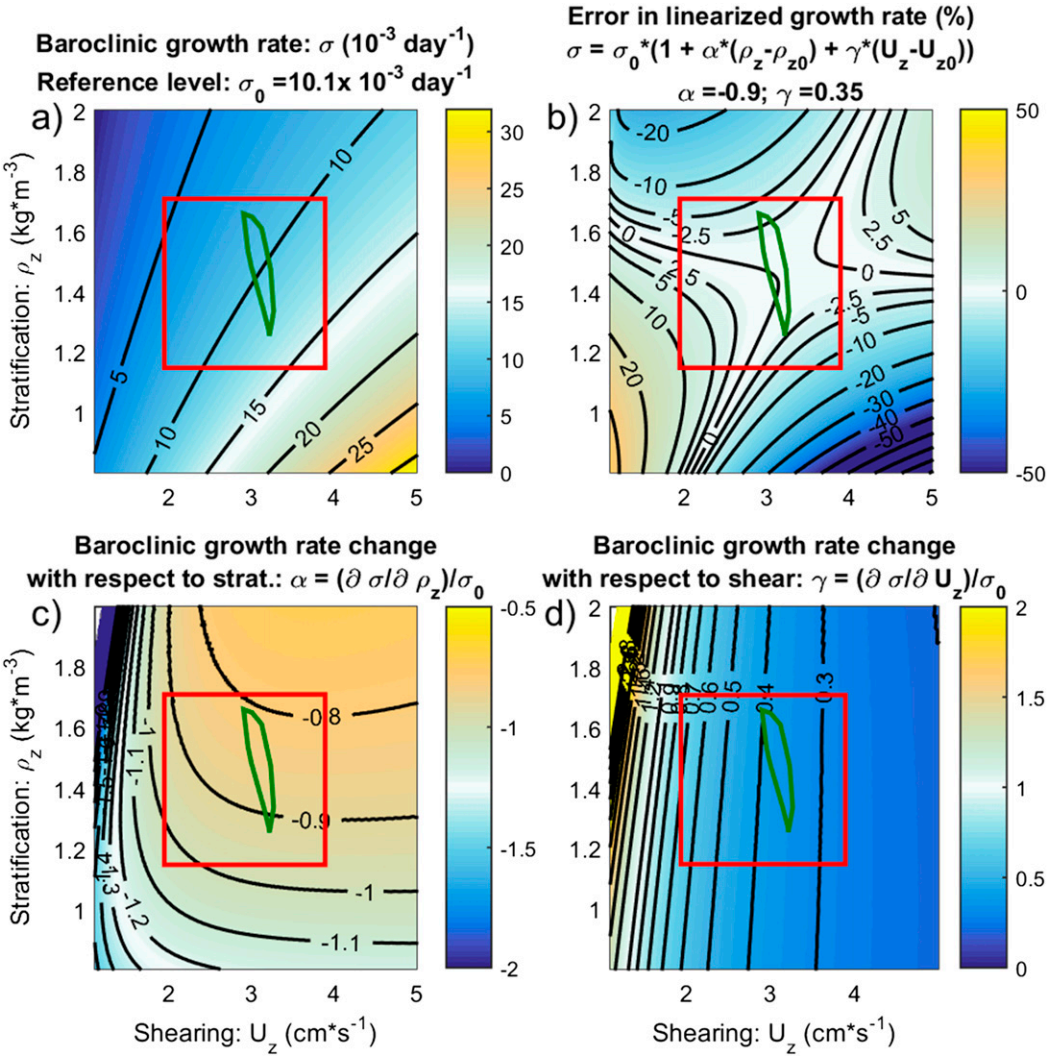

FIG. 7. Baroclinic instability growth rates over a range of shearing and stratification states. In all plots, the red box indicates the range of average seasonal values across the region. The green line indicates the area-averaged seasonal cycle of shearing and stratification. (a) Baroclinic growth rates. (b) The percent error in a linearized baroclinic growth rate, using a Taylor series expansion. The reference values are $\sigma_0 = 10.1 \times 10^{-3}\,\mathrm{day}^{-1}$, $U_{z0} = 3.1\,\mathrm{cm\,s}^{-1}$, and $\rho_{z0} = 1.45\,\mathrm{kg\,m}^{-3}$. Relative change in baroclinic growth with respect to (c) stratification and (d) shear.

following section. Figure 7b shows the percent error of the linearized growth rate, as given by Eq. (2), away from the original, nonlinear growth rate. As can be seen in Fig. 7b, the error is within ±2.5% for most possible STCC–SEC ocean states and only exceeds ±5% in the most extreme states of high (low) shearing and low (high) stratification combinations. This low level of error gives confidence that this linearization of the baroclinic growth rate can be used to simplify the nonlinear calculation and to give estimates of the relative importance of each parameter.

By using the linearization parameters and the range of variability for the shear and stratification, we can estimate how much the baroclinic growth rate will change. Based upon fluctuations in shear of $\pm 0.5\,\mathrm{cm\,s}^{-1}$ and a shearing parameter $\gamma = 0.35$, we can expect changes in the growth rate of $1.77 \times 10^{-3}\,\mathrm{day}^{-1}$ or 17.5% percent of the reference baroclinic growth rate. Stratification fluctuations of $\pm 0.1\,\mathrm{kg\,m}^{-3}$ and a stratification parameter $\alpha = -0.9$ indicates that the baroclinic growth rate would vary by $\mp 0.91 \times 10^{-3}\,\mathrm{day}^{-1}$ or 9% of the reference baroclinic growth rate. If the variation by the two parameters is assumed to be in phase and positively correlated, it can be expected that the maximum possible variability in the baroclinic growth rate would be $\pm 2.68 \times 10^{-3}\,\mathrm{day}^{-1}$ or 26.5% of the reference growth rate. In the case of this maximum total variability, 66% would be caused by variations in shear and 34% would be

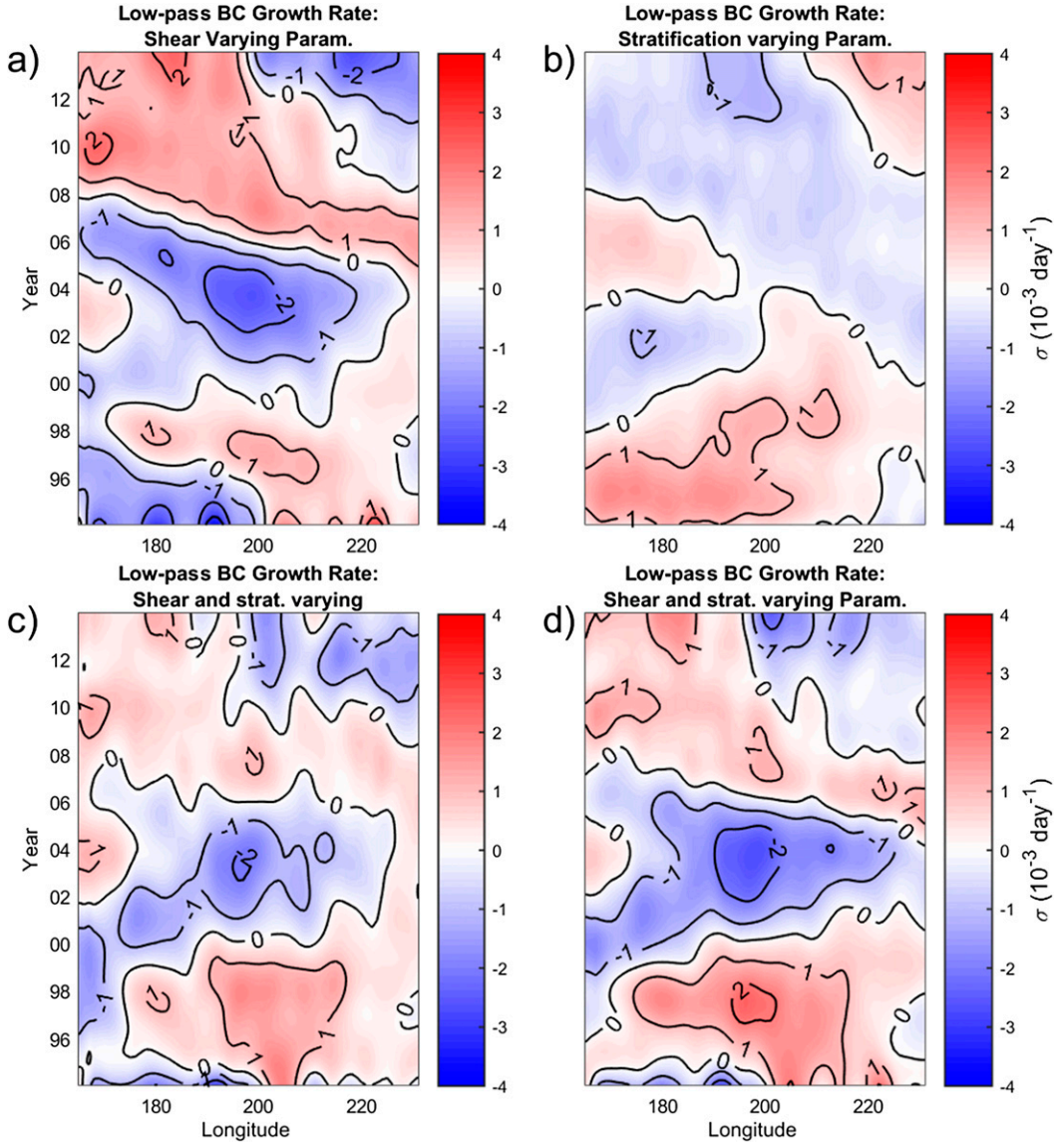

FIG. 8. Meridionally averaged bands of baroclinic instability growth rates. The upper row shows the baroclinic growth rate variability, assuming holding a parameter constant. (a) Assuming fixed stratification and allowing shear to vary. (b) Assuming fixed shear and allowing stratification to vary. (c) Fully nonlinear baroclinic growth rates. (d) Baroclinic growth rates using the linearized growth rate.

caused by variations in stratification. However, the variations do not necessarily occur in phase with each other.

When the variations by each parameter are taken as a fraction of the total variability, we find that they contribute in significantly different proportions. Figure 8 shows the baroclinic growth anomalies as caused individually by the shear (Fig. 8a) and stratification (Fig. 8b) parameters. In the early part of the data record, from 1994 to 1999, both the shear and stratification are contributing to create particularly high baroclinic growth rate anomalies. In the middle of the record, from 2000 to 2006, the shearing is particularly weak, whereas the stratification variability shows only slight departures from the mean state. The weak shear state is the primary driver of the low baroclinic growth rates. Finally, during the time period of 2007–13, the two parameters are mostly working to counteract each other. For a large portion of the region, there is high shearing but also high stratification. During this time, the shearing would cause a tendency toward particularly high growth rates, but the stratification negates at least part of that variability, and the STCC–SEC region experiences only slightly elevated growth rates.

When the linearized baroclinic growth rate is compared to the fully nonlinear calculated baroclinic growth rates, there is a high agreement, with a correlation of 0.86 (Figs. 8c,d). Overall, the character of the two signals matches well, with the periods of highs and lows in the linearized version corresponding to those in the nonlinear version. The magnitudes of variation in the linear growth rates are higher than in the nonlinear growth rates. The largest discrepancies occur in the central STCC–SEC region from approximately 180°–200°E. As this region corresponds to some of the highest mean shear in the STCC–SEC region, it would be a more significant departure from the reference state used to linearize the growth rate, and it would be expected that the linearization would overestimate these growth rates.

The low-frequency variability of the baroclinic growth rate, as shown in Fig. 8c, and the low-pass EKE signal, as shown in Fig. 4a, show excellent agreement. There is relatively high correlation of 0.66 between the two signals. The patterns of highs and lows are very similar. In describing both the baroclinic growth rate and the eddy kinetic energy patterns, it can be said that there is widely elevated signal from 1994 to 1999, followed by a depressed signal from 2000 to 2006. From 2007 to 2014, there is a rebound in the west, while the east has a slight positive anomaly between 2005 and 2007 before returning to a negative period.

5. Summary and discussion

Using more than two decades of satellite altimetry data, the low-frequency spatial–temporal patterns of EKE variability are described. The combined use of ECMWF ORAS4 ocean reanalysis data for an extended data record and gridded Argo float data for verification purposes provides a record of the subsurface state of the ocean. These data are used to calculate the theoretical strength of baroclinic instabilities in an idealized 2.5-layer system, which are believed to be the cause of the eddy activity in the STCC–SEC region. Through the linearization of the dominant parameters affecting the strength of the instabilities, it is found that the changes in the shearing and stratification of the STCC–SEC system are both significant. In the range of maximum variability, the effect of changing shear would be roughly twice as large as that of changing stratification.

Further examination of the state of the STCC–SEC region allows the relative effects of changing temperature and salinity to be explored. The relative effect on changing stratification is seen directly through the change in density fields. Changes in the shear are found by using a thermal wind balance on the linearized state equation and integrating through the layer depth. When the parameters are compared, the contribution of salinity variability is approximately 50%–75% of the temperature variability for both the stratification and shear.

A number of papers have explored the variability in the South Pacific caused by the gyre spinup. The increased wind stress curl over the larger ocean is found to have a clear effect on sea level trends (Qiu and Chen 2006; Roemmich et al. 2007; Sasaki et al. 2008; among others). Baroclinic Rossby wave adjustment to the changing basin-scale wind stress curl is largely able to account for the observed sea surface height variability (Qiu and Chen 2006); however, the one region where these dynamics break down is in the STCC–SEC region. Nevertheless, the decadal patterns of temperature variability agree well with the local sea surface height variability and exhibit features of Rossby wave propagation. In agreement with Chelton and Schlax (1996) and Wang et al. (1998), the observed propagation speed is roughly 6.5 $\mathrm{cm\,s^{-1}}$ and exceeds that predicted by linear theory. In further investigating sea level trends in the region, Bowen et al. (2006) were able to find that a combination of local wind and heat forcing are able to explain between 40% and 60% of the sea surface height variability. However, a large portion of this variability remains unexplained. Eddy activity could be a driver of this variability. Indeed, in the North Pacific, it has been shown by Qiu et al. (2015) that eddy activity can be a significant driver of regional sea level variability. If a similar dynamic exists in the South Pacific, it is fair to expect the low-frequency variability of eddy activity in the STCC–SEC region to impact the regional sea level change. Future work will be needed to investigate this change.

Greatbatch et al. (2010) looked into the effect of eddy-driven transport in the Gulf Stream region and found that the eddy momentum fluxes can be a significant driver of circulation. While the South Pacific STCC would have a weaker forcing, it is possible that the eddy activity in the STCC–SEC band has a similar effect on transport in the region. An investigation of this circulation feature could help to explain the transports in the region and how they relate to the larger, wind-driven gyre circulation.

There are likely many connections to forcings from the atmosphere, with many varied effects. Kessler and Gourdeau (2007) found that linear wind forcing can explain annual thermocline depth variability in the southwest interior South Pacific through Rossby wave dynamics. Additionally, local wind stress forcing can cause anomalous Ekman pumping/suction. Morris et al. (1996) used this framework to explore the annual density variability, although Kessler and Gourdeau (2007) note that this does not preclude the presence of

Rossby waves. If significant, the decadal variability of the strength of this local forcing could be a factor in the changing state of the waters of the STCC–SEC region. A number of papers (Martinez et al. 2009; Montecinos and Pizarro 2005; Hill et al. 2011; among others) have looked at the effect of large, basin-scale forcings and their impact on circulation and the state of the ocean across the South Pacific and, in some cases, their connection to various climate indices. For example, Cai (2006) and Roemmich et al. (2007) examine the connection of the larger South Pacific Gyre spinup to the southern annual mode (SAM), while Sasaki et al. (2008) explore the connection to ENSO-like variability. Zilberman et al. (2014) looked into the effect of the SAM on midlatitude meridional transport, which could directly affect the STCC–SEC region by advecting anomalous waters into the region. Additionally, the same indices could have changes on local forcing. Zhang and Qu (2014) showed connections of sea surface salinity variability to the shifting of the South Pacific convergence zone (SPCZ) by altering evaporation–precipitation patterns, and this connection to the PDO. The shifting of the SPCZ could have local forcing through changes in sea surface salinity and temperature and through local wind forcing (Ganachaud et al. 2014).

Last, further work is also needed to investigate the topographic influence on the region. As noted in the introduction, within the STCC–SEC region, there are hot spots of eddy activity that correspond well with topographic features such as the Kermadec Ridge. These are also the regions in which there is weaker correspondence between variability in the eddy activity and variability in the strength of baroclinic instabilities. The strong topographic features, with some peaks extending to less than 500 m below the surface, could have steering effects on the circulation of the region. Additionally, these sites could be sources of wave generation (Anderson and Killworth 1977) or even eddy disruption, dissipation, or reorganization (Adcock and Marshall 2000, Dewar 2002). The connection of these direct topographic influences as well as the connections to larger atmospheric forcings would give greater insight into the character of these eddy activity variations and the role they play in the larger South Pacific oceanic variability.

Acknowledgments. The authors acknowledge support from NASA's OSTST program (NNX13AD91G). The altimeter products were produced by Ssalto/Duacs and distributed by AVISO, with support from CNES (http://www.aviso.altimetry.fr/duacs/). We also acknowledge ECMWF for providing the ORAS4 reanalysis data and JAMSTEC for providing the Argo MOAA GPV data.

REFERENCES

Adcock, S. T., and D. P. Marshall, 2000: Interactions between geostrophic eddies and the mean circulation over large-scale bottom topography. *J. Phys. Oceanogr.*, **30**, 3223–3238, doi:10.1175/1520-0485(2000)030<3223:IBGEAT>2.0.CO;2.

Anderson, D. L., and P. D. Killworth, 1977: Spin-up of a stratified ocean, with topography. *Deep-Sea Res.*, **24**, 709–732, doi:10.1016/0146-6291(77)90495-7.

Balmaseda, M. A., K. Mogensen, and A. T. Weaver, 2013: Evaluation of the ECMWF ocean reanalysis system ORAS4. *Quart. J. Roy. Meteor. Soc.*, **139**, 1132–1161, doi:10.1002/qj.2063.

Bowen, M. M., P. J. Sutton, and D. Roemmich, 2006: Wind-driven and steric fluctuations of sea surface height in the southwest Pacific. *Geophys. Res. Lett.*, **33**, L14617, doi:10.1029/2006GL026160.

Cai, W., 2006: Antarctic ozone depletion causes an intensification of the Southern Ocean super-gyre circulation. *Geophys. Res. Lett.*, **33**, L03712, doi:10.1029/2005GL024911.

Chelton, D. B., and M. G. Schlax, 1996: Global observations of oceanic Rossby waves. *Science*, **272**, 234–238, doi:10.1126/science.272.5259.234.

De Szoeke, R., 1987: On the wind-driven circulation of the South Pacific Ocean. *J. Phys. Oceanogr.*, **17**, 613–630, doi:10.1175/1520-0485(1987)017<0613:OTWDCO>2.0.CO;2.

Dewar, W. K., 2002: Baroclinic eddy interaction with isolated topography. *J. Phys. Oceanogr.*, **32**, 2789–2805, doi:10.1175/1520-0485(2002)032<2789:BEIWIT>2.0.CO;2.

Ducet, N., P.-Y. Le Traon, and G. Reverdin, 2000: Global high-resolution mapping of ocean circulation from TOPEX/Poseidon and ERS-1 and-2. *J. Geophys. Res. Oceans*, **105**, 19 477–19 498, doi:10.1029/2000JC900063.

Ganachaud, A., and Coauthors, 2014: The Southwest Pacific Ocean Circulation and Climate Experiment (SPICE). *J. Geophys. Res. Oceans*, **119**, 7660–7686, doi:10.1002/2013JC009678.

Greatbatch, R., X. Zhai, M. Claus, L. Czeschel, and W. Rath, 2010: Transport driven by eddy momentum fluxes in the Gulf Stream extension region. *Geophys. Res. Lett.*, **37**, L24401, doi:10.1029/2010GL045473.

Hill, K., S. Rintoul, K. Ridgway, and P. Oke, 2011: Decadal changes in the South Pacific western boundary current system revealed in observations and ocean state estimates. *J. Geophys. Res.*, **116**, C01009, doi:10.1029/2009JC005926.

Hosoda, S., T. Ohira, and T. Nakamura, 2008: A monthly mean dataset of global oceanic temperature and salinity derived from Argo float observations. *JAMSTEC Rep. Res. Dev.*, **8**, 47–59, doi:10.5918/jamstecr.8.47.

IPCC, 2013: *Climate Change 2013: The Physical Science Basis*. Cambridge University Press, 1535 pp.

Kessler, W. S., and L. Gourdeau, 2007: The annual cycle of circulation of the southwest subtropical Pacific, analyzed in an ocean GCM. *J. Phys. Oceanogr.*, **37**, 1610–1627, doi:10.1175/JPO3046.1.

Luyten, J., J. Pedlosky, and H. Stommel, 1983: The ventilated thermocline. *J. Phys. Oceanogr.*, **13**, 292–309, doi:10.1175/1520-0485(1983)013<0292:TVT>2.0.CO;2.

Martinez, E., A. Ganachaud, J. Lefèvre, and K. Maamaatuaiahutapu, 2009: Central South Pacific thermocline water circulation from a high-resolution ocean model validated against satellite data: Seasonal variability and El Niño 1997–1998 influence. *J. Geophys. Res.*, **114**, C05012, doi:10.1029/2008JC004824.

Merle, J., H. Rotschi, and B. Voituriez, 1969: Zonal circulation in the tropical western South Pacific at 170°E. *Bull. Japan Soc.*

Fish. Oceanogr., Special Issue (Prof. Uda's Commemorative Papers), 91–98.

Montecinos, A., and O. Pizarro, 2005: Interdecadal sea surface temperature–sea level pressure coupled variability in the South Pacific Ocean. *J. Geophys. Res.*, **110**, C08005, doi:10.1029/2004JC002743.

Morris, M., D. Roemmich, and B. Cornuelle, 1996: Observations of variability in the South Pacific Subtropical Gyre. *J. Phys. Oceanogr.*, **26**, 2359–2380, doi:10.1175/1520-0485(1996)026<2359:OOVITS>2.0.CO;2.

Qiu, B., 1999: Seasonal eddy field modulation of the North Pacific Subtropical Countercurrent: TOPEX/Poseidon observations and theory. *J. Phys. Oceanogr.*, **29**, 2471–2486, doi:10.1175/1520-0485(1999)029<2471:SEFMOT>2.0.CO;2.

——, and S. Chen, 2004: Seasonal modulations in the eddy field of the South Pacific Ocean. *J. Phys. Oceanogr.*, **34**, 1515–1527, doi:10.1175/1520-0485(2004)034<1515:SMITEF>2.0.CO;2.

——, and ——, 2006: Decadal variability in the large-scale sea surface height field of the South Pacific Ocean: Observations and causes. *J. Phys. Oceanogr.*, **36**, 1751–1762, doi:10.1175/JPO2943.1.

——, ——, L. Wu, and S. Kida, 2015: Wind- versus eddy-forced regional sea level trends and variability in the North Pacific Ocean. *J. Climate*, **28**, 1561–1577, doi:10.1175/JCLI-D-14-00479.1.

Qu, T., and E. J. Lindstrom, 2002: A climatological interpretation of the circulation in the western South Pacific. *J. Phys. Oceanogr.*, **32**, 2492–2508, doi:10.1175/1520-0485-32.9.2492.

Reid, J. L., 1986: On the total geostrophic circulation of the South Pacific Ocean: Flow patterns, tracers and transports. *Prog. Oceanogr.*, **16**, 1–61, doi:10.1016/0079-6611(86)90036-4.

Roemmich, D., J. Gilson, R. Davis, P. Sutton, S. Wijffels, and S. Riser, 2007: Decadal spinup of the South Pacific Subtropical Gyre. *J. Phys. Oceanogr.*, **37**, 162–173, doi:10.1175/JPO3004.1.

Sasaki, Y. N., S. Minobe, N. Schneider, T. Kagimoto, M. Nonaka, and H. Sasaki, 2008: Decadal sea level variability in the South Pacific in a global eddy-resolving ocean model hindcast. *J. Phys. Oceanogr.*, **38**, 1731–1747, doi:10.1175/2007JPO3915.1.

Schneider, W., M. Fukasawa, J. Garcés-Vargas, L. Bravo, H. Uchida, T. Kawano, and R. Fuenzalida, 2007: Spin-up of South Pacific Subtropical Gyre freshens and cools the upper layer of the eastern South Pacific Ocean. *Geophys. Res. Lett.*, **34**, L15608, doi:10.1029/2006GL028842.

Tsuchiya, M., 1982: On the Pacific upper-water circulation. *J. Mar. Res.*, **40**, 777–799.

Wang, L., C. Koblinsky, S. Howden, and B. Beckley, 1998: Large-scale Rossby wave in the mid-latitude South Pacific from altimetry data. *Geophys. Res. Lett.*, **25**, 179–182, doi:10.1029/97GL03567.

Wyrtki, K., 1975: Fluctuations of the dynamic topography in the Pacific Ocean. *J. Phys. Oceanogr.*, **5**, 450–459, doi:10.1175/1520-0485(1975)005<0450:FOTDTI>2.0.CO;2.

Zhang, L., and T. Qu, 2014: Low-frequency variability of South Pacific Tropical Water from Argo. *Geophys. Res. Lett.*, **41**, 2441–2446, doi:10.1002/2014GL059490.

——, and ——, 2015: Low-frequency variability of the South Pacific Subtropical Gyre as seen from satellite altimetry and Argo. *J. Phys. Oceanogr.*, **45**, 3083–3098, doi:10.1175/JPO-D-15-0026.1.

Zilberman, N., D. Roemmich, and S. Gille, 2014: Meridional volume transport in the South Pacific: Mean and SAM-related variability. *J. Geophys. Res. Oceans*, **119**, 2658–2678, doi:10.1002/2013JC009688.